Supporting Information: Analysis of Keratinocytic Exosomes from Diabetic and Non-Diabetic Mice by Charge Detection Mass Spectrometry

Brooke A. Brown[1], Poornachander R. Guda[2], Xuyao Zeng[1], Adam Anthony[1], Andrew Couse[1], Lauren F. Barnes[1], Edie M. Sharon[1], Jonathan C. Trinidad[1], Chandan K. Sen[2], Martin F. Jarrold[1], Subhadip Ghatak[2], and David E. Clemmer[1]*

[1]*Department of Chemistry, Indiana University, Bloomington Indiana 47505 USA*

[2] *Indiana Center for Regenerative Medicine & Engineering, Department of Surgery, Indiana University School of Medicine, Indianapolis, IN, USA*

Supplementary experimental procedures

Nanoparticle tracking analysis. Exosome diameters and concentrations were characterized using a NanoSight NS300 with a 532 nm laser and scientific complementary metal-oxide-semiconductor (SCMOS) camera (Malvern Instruments, Worcestershire, UK) as previously described.[22,23] Sample dilution was as needed in fresh milliQ water to obtain 5-100 particles/frame. The syringe pump was set to a speed of 60. The camera level was set at 15 and the detection threshold was set at 5. Five video runs of 30 s were carried out for each sample. Data were analyzed by NTA 3.0 software (Malvern Instruments, Worcestershire, UK).

Immunohistochemistry and microscopy. Immunohistochemistry (IHC) was performed as described previously[24]. All antibodies were purchased from Abcam (Abcam, Waltham, MA) Immunostainings of hnRNP Q (ab184946; 1:100) were performed on cryosections of wound-edge tissue. Briefly, the sections were blocked with 10% normal goat serum and incubated with hnRNP Q primary antibody overnight at 4 °C. Signal was visualized by subsequent incubation with fluorescence-tagged secondary antibodies (Alexa 568-tagged α-rabbit, 1:200) and counterstained with 4',6-diamidino-2-phenylindole (DAPI). Images were captured by microscope using Axio Scan.Z1 (Zeiss, Oberkochen, Germany). A statistical analysis of these data was performed using the GraphPad Prism v8.0 (GraphPad Software, San Diego, CA) suite of software. Statistical analyses between groups were performed using unpaired Student's two-sided t tests. Values of $P < 0.05$ were considered statistically significant.

Gaussian mixture model. A Gaussian mixture model with expectation maximization (GMM) algorithm was performed in Anaconda (Anaconda Software Distribution, Austin, TX). The GMM algorithm is described in detail elsewhere.[1,5] Briefly, a GMM is a parametric probability density function represented as a weighted sum of Gaussian component densities. A mixture model

(p) is the weighted sum of a number (k) of probability distribution functions. For a 2D analysis, a GMM mixture is defined by the sum of bivariate normal distributions (N):

$$p(x \mid \boldsymbol{\mu},\boldsymbol{\sigma}) = \sum_{i\epsilon[0,k)} \pi_i N(x,\mu_i,\sigma_i) \qquad \text{(Eq. 1).}$$

Where μ and σ are the mean vector and covariance of the kth Gaussian, respectively. The parameters μ_i,σ_i and the weights π_i for the components are an attempt to fit the population x composed of N features. The expectation maximization algorithm minimizes the negative loglikelihood and determines the set of parameters which define the best mixture model $\hat{p}(x \mid \boldsymbol{\mu},\boldsymbol{\sigma})$.

By fitting a GMM to a given dataset, an individual mode of the probability distribution can be characterized by its mean and covariance. Following the GMM fit, the expectation maximization algorithm determines the best fit over a user-defined number of iterations. Initially, the expectation checks to see which mode each data point most probably belongs to by calculating values of responsibilities $[r(i \mid x_j)]$ using the expression:

$$r(i \mid x_j) = \frac{\pi_i N(x_i \mid \mu,\sigma)}{\sum_{j\epsilon[0,k)} \pi_j N(x_i \mid \mu_j,\sigma_j)} \qquad \text{(Eq. 2).}$$

This means that each data point has a probability of being ascribed to each of the subpopulations that is determined by GMM for the mixture. Once responsibilities are assigned to each data point, criteria must be met to assign each data point to an optimal component of the Gaussian mixture model. This is accomplished by the maximization step, where the responsibilities are updated to determine how much each point contributes to multiple Gaussian distributions:

$$\mu_i^{new} = \frac{1}{N_c} \sum_i r(i \mid x_j) x_i \, . \qquad \text{(Eq. 3).}$$

The standard deviation assigned to each data point is also updated, such that the GMM algorithm allows us to determine the best parameters of the model with a given number of modes. However, because the number of components into which the data separates is unknown, it is necessary to have additional screening for optimal assignments. This is accomplished by comparing the negative loglikelihood and Bayesian information criterion (BIC) to the GMM output. This criterion gives us an estimation of how good the GMM is by the fitness of the model (loglikelihood) and the model complexity. A lower BIC indicates a better fit. We performed multiple GMM fits on each given data set where the bounds for the possible number of components were floated, allowing the GMM, negative loglikelihood, and BIC to find the global optimum for each component as well as the most probable number of components based on our previously described criteria.

Electron microscopy. Electron microscopy (EM) measurements were used to characterize the size distributions of exosome particles. In this approach, a 300 μm mesh of carbon-coated copper grids were subjected to a glow-discharge treatment prior to sample loading. A 2.0 μL aliquot of each EV sample (also analyzed by CDMS and MS-based proteomics measurements, see below) was spotted over the entire grid area. After ~30 s, excess solvent was removed by blotting with filter paper. The grids were then stained for 30 s with 2% uranyl acetate. After drying, the grids were imaged on a JEOL JEM 1400 plus transmission electron microscope equipped with a 4000×4000-pixel Gatan charge-coupled device (CCD) camera. Individual particle diameters were determined using the ImageJ imaging software to determine the Feret's diameter as described previously.[25,26]

Preparation of samples for proteomics analyses. Samples of both non-diabetic and diabetic murine **Exo$_{\kappa}$** were also subjected to a liquid chromatography (LC)-MS-database search proteomics

analysis to assess what proteins were present in the samples. For these analyses, aliquots of each sample were dried, dissolved in 8 M urea, and preconcentrated through a 30 kDa Amicon Ultra-15 molecular weight cut off filter (Millipore Sigma, Burlington, MA). Protein disulfide bonds from concentrated samples were reduced with 2 mM tris(2-carboxyethyle)-phosphine hydrochloride (Sigma Aldrich, St. Louis, MO) for 1 h at 56 ˚C. Reduced proteins were alkylated with 4 mM iodoacetamide (Sigma Aldrich, St. Louis, MO) for 45 min in the dark at room temperature. The urea concentration was diluted to 1 M using a prepared 100 mM ammonium bicarbonate buffer (pH = 7.5) (Sigma Aldrich, St. Louis, MO) and modified sequencing grade trypsin (Promega, Madison, WI) was added at a 1:100 enzyme:protein ratio. Trypsin digestion was allowed to progress overnight at 37 ˚C. After digestion, peptides were desalted using a C-18 preparative Sep-Pak cartridge (Waters, Milford, MA).

LC-MS-database search proteomics characterization. Desalted peptides were resolubilized in buffer A (0.1% formic acid in water) (Fisher Scientific, Hampton, NH) and loaded onto a reverse-phase trap column (Acclaim PepMap 100, 75 μm × 2 cm, nano viper, C18, 3 μm, 100 Å) (ThermoFisher, Waltham, MA) by an easyNanoLC 1200 (ThermoFisher, Waltham, MA) at a flow rate of 5 $\mu L \cdot min^{-1}$ for 2 min. Peptides were resolved using an analytical reversed-phase column (Acclaim PepMap RSLC, 75 μm diameter × 25 cm in length, 2 μm diameter beads with an average pore size of 100 Å) (ThermoFisher, Waltham, MA) over a 120-min linear gradient from 7% to 38% buffer B (0.1 % formic acid, 80% acetonitrile, 20% water) (Fisher Scientific, Hanover, NH). Peptides eluting from the analytical column were electrosprayed into a Fusion Lumos Tribrid (Thermo Fisher, Waltham, MA). Precursor ions were monitored with a resolving power of 120000 (@ 200 m/z). Individual precursors (z = 2 to 7) were selected using the quadrupole offset from the monoisotopic mass by 0.5 m/z with a window of 2 m/z. Peptides were subjected to high energy

collision-induced dissociation (30 ± 5%) and fragment ion masses were measured with a resolving power of 15000 (@ 200 *m*/*z*). The automatic gain control (AGC) target was set to 2.0×10^5 or a fill time of 200 ms. Peptide database searching was completed using Proteome Discoverer 2.1 (Thermo Fisher, Waltham, MA) against the UniprotKB Mus musculus database (Download Date: 2021-Jun-4) with a precursor mass accuracy of 10 ppm and a product ion mass accuracy of 0.02 Da. Observed modifications include methionine oxidation, N-terminal pyroglutamate, N-terminal acetylation, N-terminal methionine loss, and cysteine carbamidomethylation. Percolator scoring was used with a 0.01 strict and 0.05 relaxed false discovery rate (FDR) based on the q-value. Proteins were manually filtered to accept only those identified using at least two peptides. Protein levels in each of the fractions were estimated using the summed signal intensities of identified peptides as automatically extracted by Proteome Discoverer 2.1.

For all proteins identified from LC-MS studies, we removed any identification that did not have at least two unique peptide assignments as well as major serum proteins (16 total). The contribution of these species to the low mass regions of the CDMS spectra is currently unknown so this elimination precludes any comparison between CDMS and proteomics data. However, it does allow for detailed examination of exosome-specific differences between sample types.To assess enrichment, the normalized abundance ratio of diabetic:non-diabetic for samples run on the same day was calculated and averaged to determine which proteins are more abundant in **Exo$_\kappa$** derived from diabetic or non-diabetic mice.

Supplementary data:

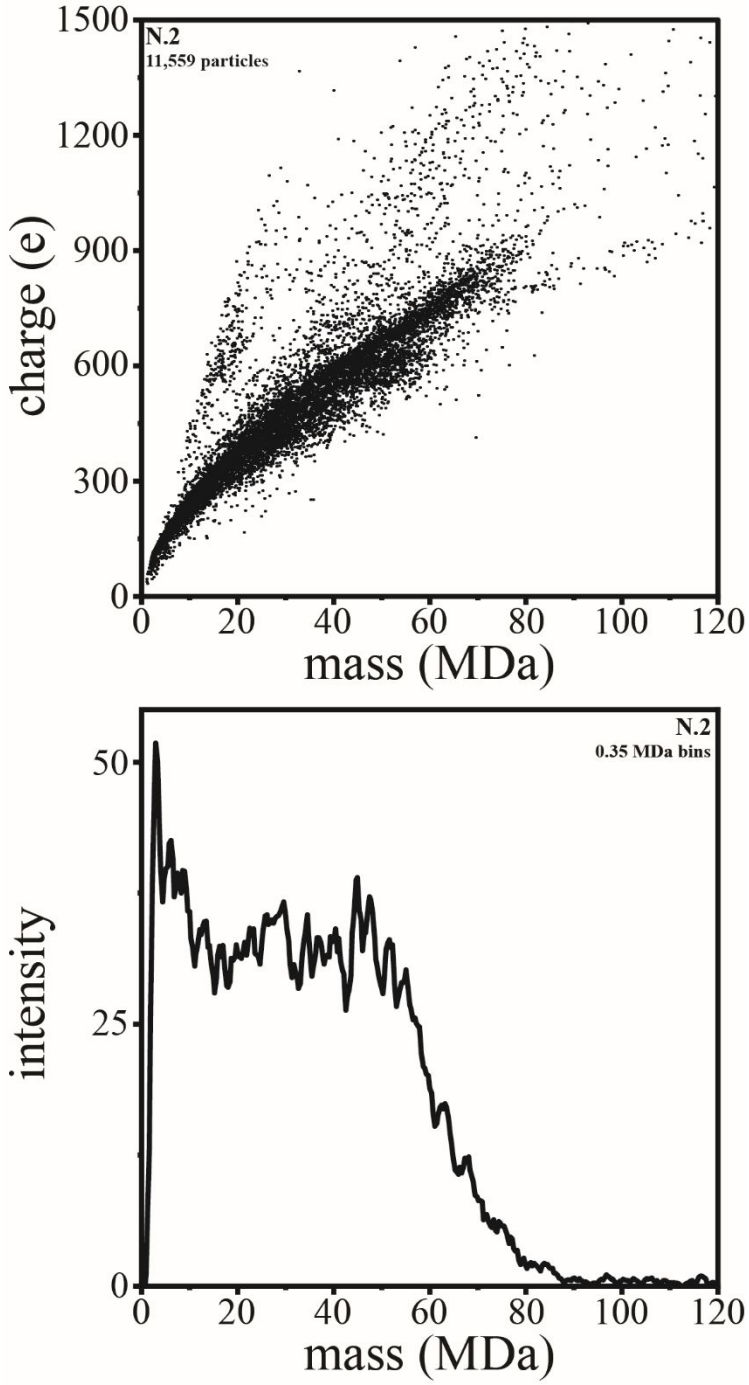

Figure S1. (Top) Mass versus charge CDMS measurement for normal (N.2) exosome sample. (Bottom) Mass spectrum generated upon integrating the ion signal across the charge dimension using 0.35 MDa bins.

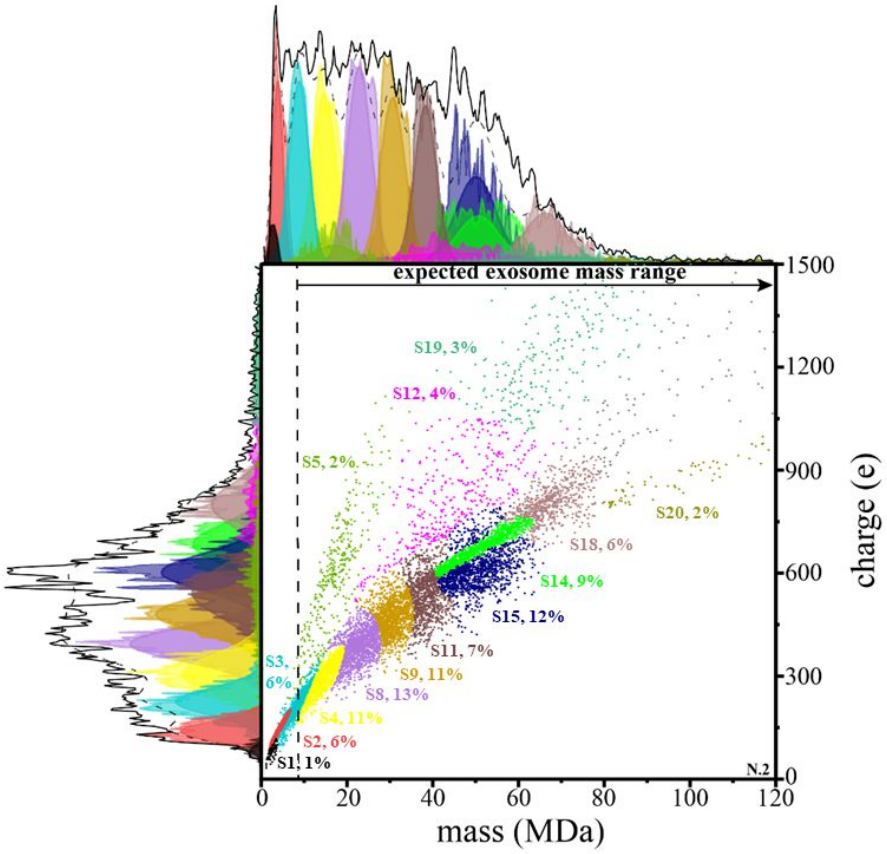

Figure S2. Two-dimensional mass versus charge plot showing subpopulations obtained from Gaussian fits to the experimental data for the N.2 CDMS measurement of normal **Exo$_K$** samples. See main text for details. This model finds evidence for fourteen subpopulations with abundances greater than 1%. Each point shows the mass and charge measured for a single particle and is assigned to a subpopulation (indicated by color). Subfamily assignment is based on the highest probability of each particle belonging to a specific subfamily. Visually, this leads to boundaries that are artificially strict as, in reality, the subpopulations overlap. The top and left side traces show the integrated raw data for the mass and charge dimensions respectively and corresponding sums of the Gaussian curves as black lines for these dimensions. The determined fits for each subpopulation are also delineated using the same color scheme. The percentage of each subpopulation is also indicated. The dashed vertical line provides an estimate of the delineation between those particles having masses in the range that is expected for exosomes and those particles that are too small to be exosomes.

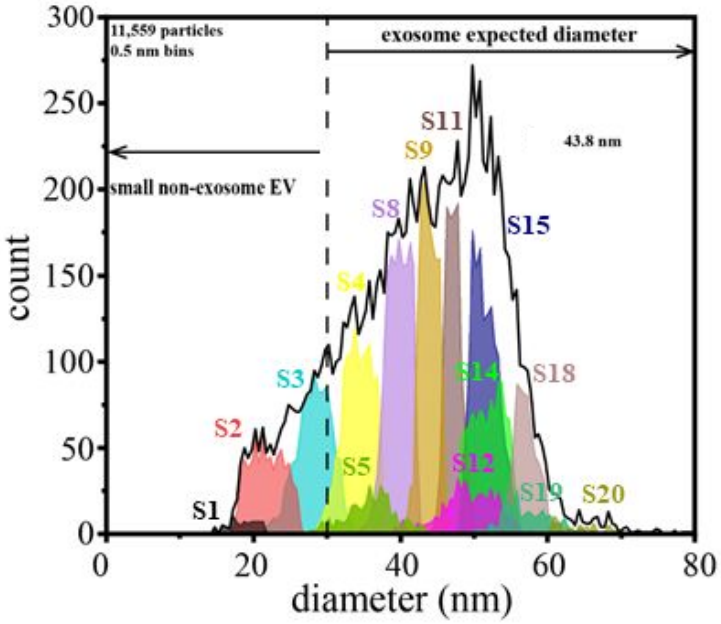

Figure S3. Plot of CDMS-derived diameters for each normal sample (N.2) subpopulation (shown in figure S2) using a bin size of 0.5 nm. Particle diameters from CDMS were determined by assuming a spherical geometry and a density of 1.17 g/mL.

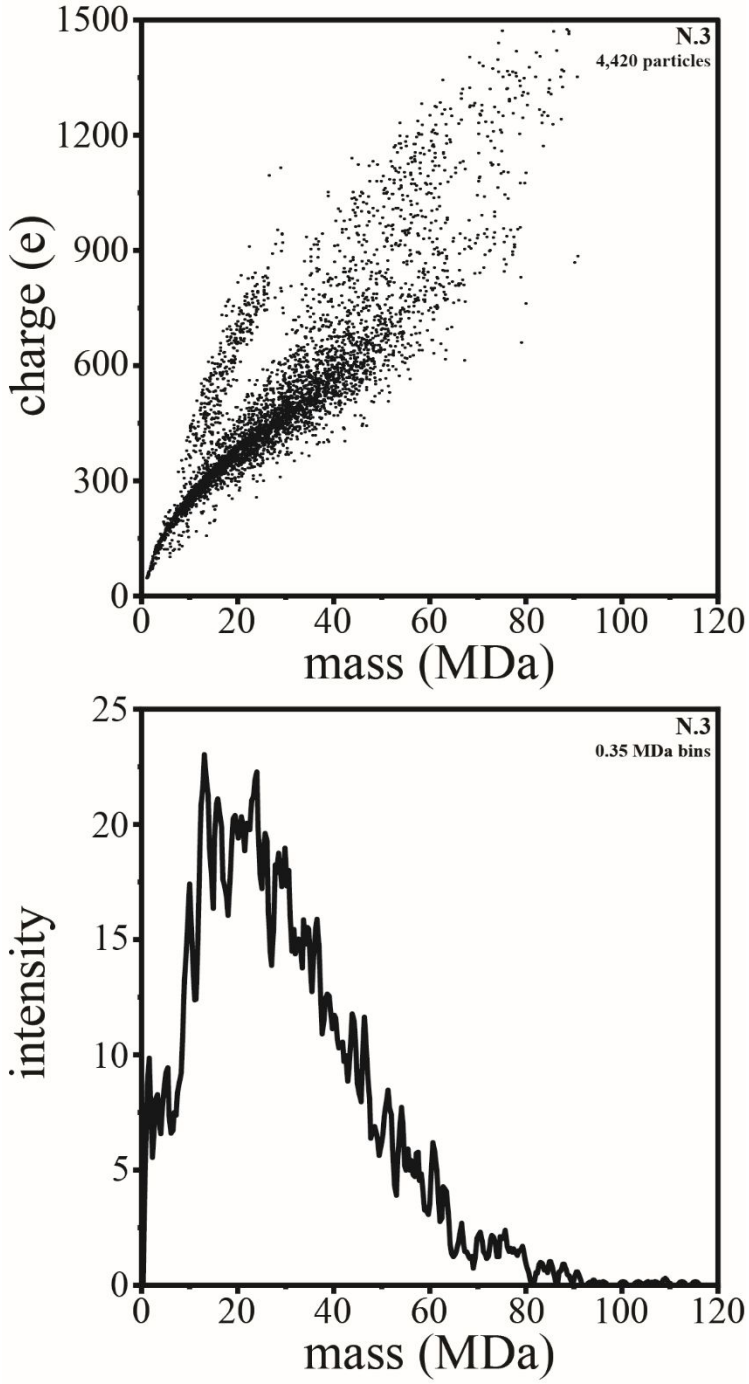

Figure S4. (Top) Mass versus charge CDMS measurement for normal (N.3) exosome sample. (Bottom) Mass spectrum generated upon integrating the ion signal across the charge dimension using 0.35 MDa bins.

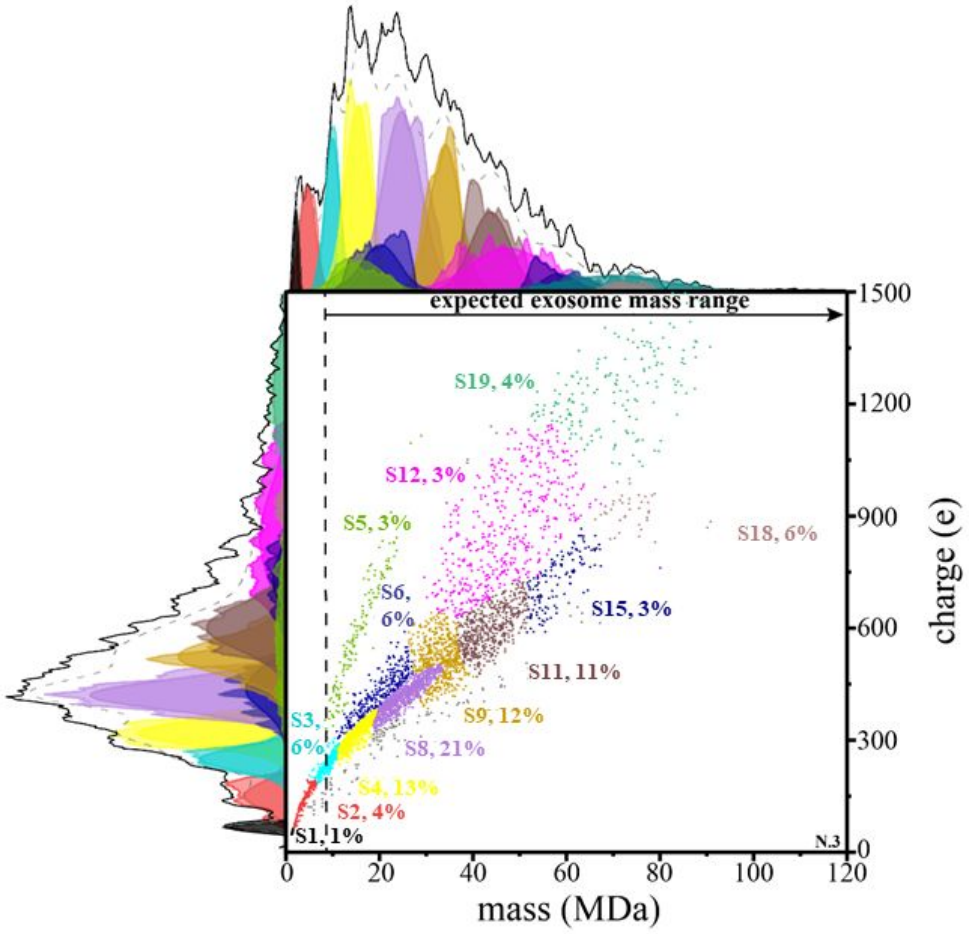

Figure S5. Two-dimensional mass versus charge plot showing subpopulations obtained from Gaussian fits to the experimental data for the third CDMS (N.3) measurement of normal **Exo$_\kappa$** samples. See main text for details. This model finds evidence for twelve subpopulations with abundances greater than 1%. Each point shows the mass and charge measured for a single particle and is assigned to a subpopulation (indicated by color). Subfamily assignment is based on the highest probability of each particle belonging to a specific subfamily. Visually, this leads to boundaries that are artificially strict as, in reality, the subpopulations overlap. The top and left side traces show the integrated raw data for the mass and charge dimensions respectively and the corresponding sums of the Gaussian curves as black lines for these dimensions. The determined fits for each subpopulation are also delineated using the same color scheme. The percentage of each subpopulation is also indicated. The dashed vertical line provides an estimate of the delineation between those particles having masses in the range that is expected for exosomes and those particles that are too small to be exosomes.

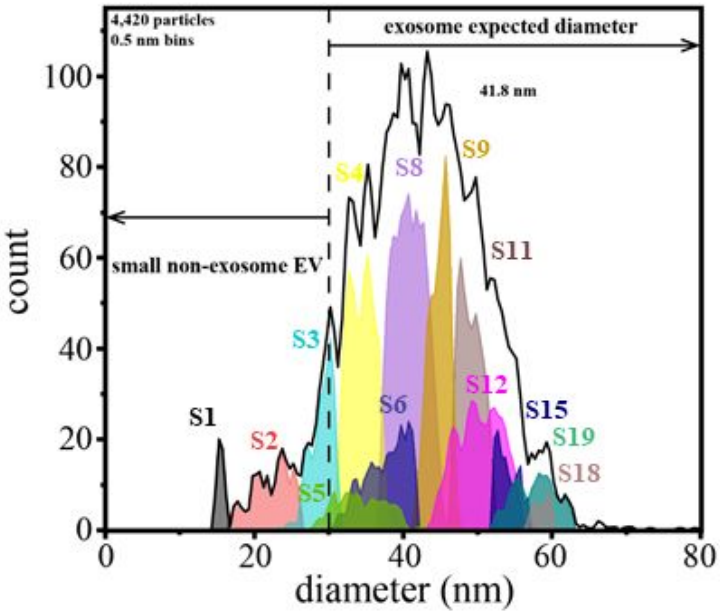

Figure S6. Plot of CDMS-derived diameters for each normal sample (N.3) subpopulation (shown in figure S5) using a bin size of 0.5 nm. Particle diameters from CDMS were determined by assuming a spherical geometry and a density of 1.17 g/mL.

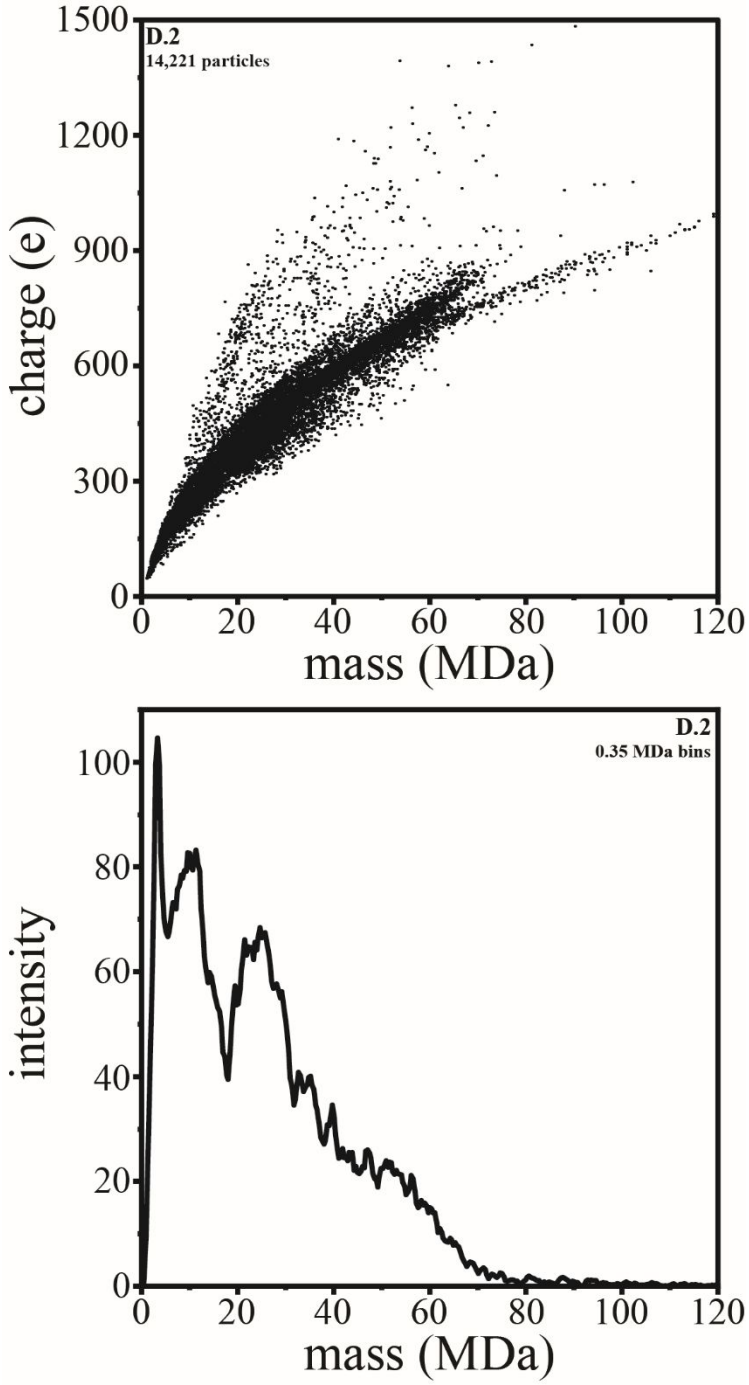

Figure S7. (Top) Mass versus charge CDMS measurement for diabetic (D.2) exosome sample. (Bottom) Mass spectrum generated upon integrating the ion signal across the charge dimension using 0.35 MDa bins.

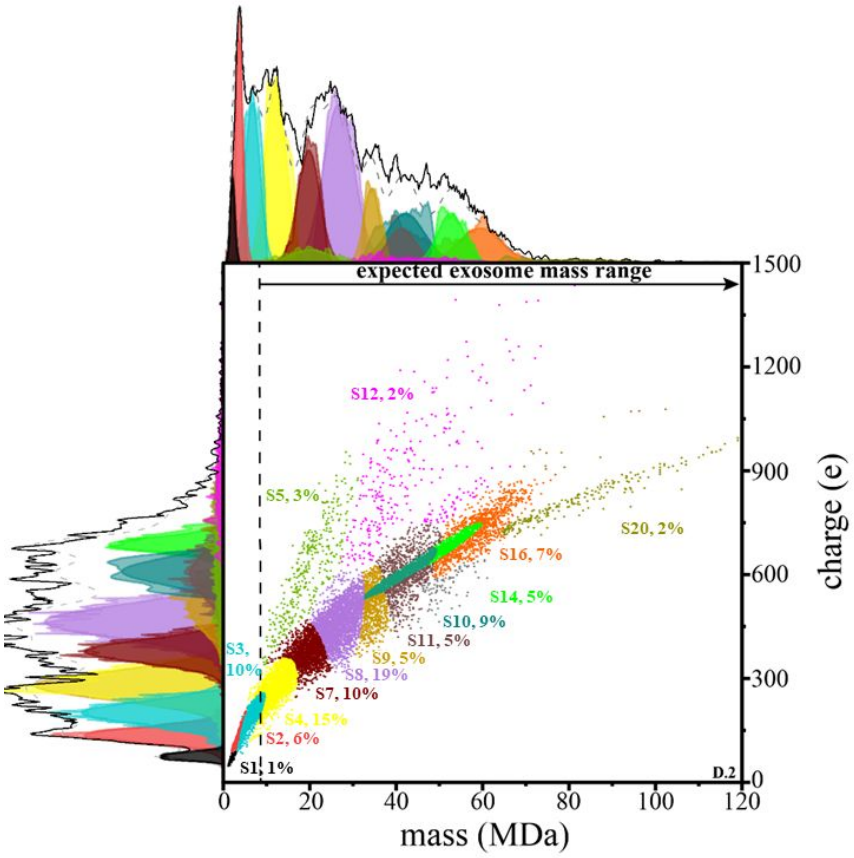

Figure S8. Two-dimensional mass versus charge plot showing subpopulations obtained from Gaussian fits to the experimental data for the second CDMS (D.2) measurement of diabetic murine **Exo$_{\kappa}$** samples. See main text for details. This model finds evidence for fourteen subpopulations with abundances greater than 1%. Each point shows the mass and charge measured for a single particle and is assigned to a subpopulation (indicated by color). Subfamily assignment is based on the highest probability of each particle belonging to a specific subfamily. Visually, this leads to boundaries that are artificially strict as in reality the subpopulations overlap. The top and left side traces show the integrated raw data for the mass and charge dimensions, respectively and the corresponding sums of the Gaussian curves as black lines for these dimensions. The determined fits for each subpopulation are also delineated using the same color scheme. The percentage of each subpopulation is also indicated. The dashed vertical line provides an estimate of the delineation between those particles having masses in the range that is expected for exosomes, and those particles that are too small to be exosomes.

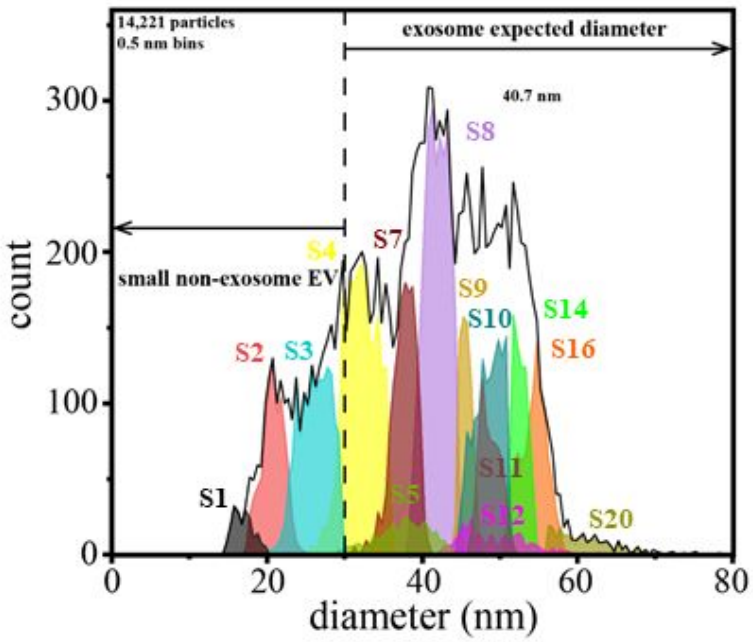

Figure S9. Plot of CDMS-derived diameters for each diabetic sample (D.2) subpopulation (shown in figure S8) using a bin size of 0.5 nm. Particle diameters from CDMS were determined by assuming a spherical geometry and a density of 1.17 g/mL.

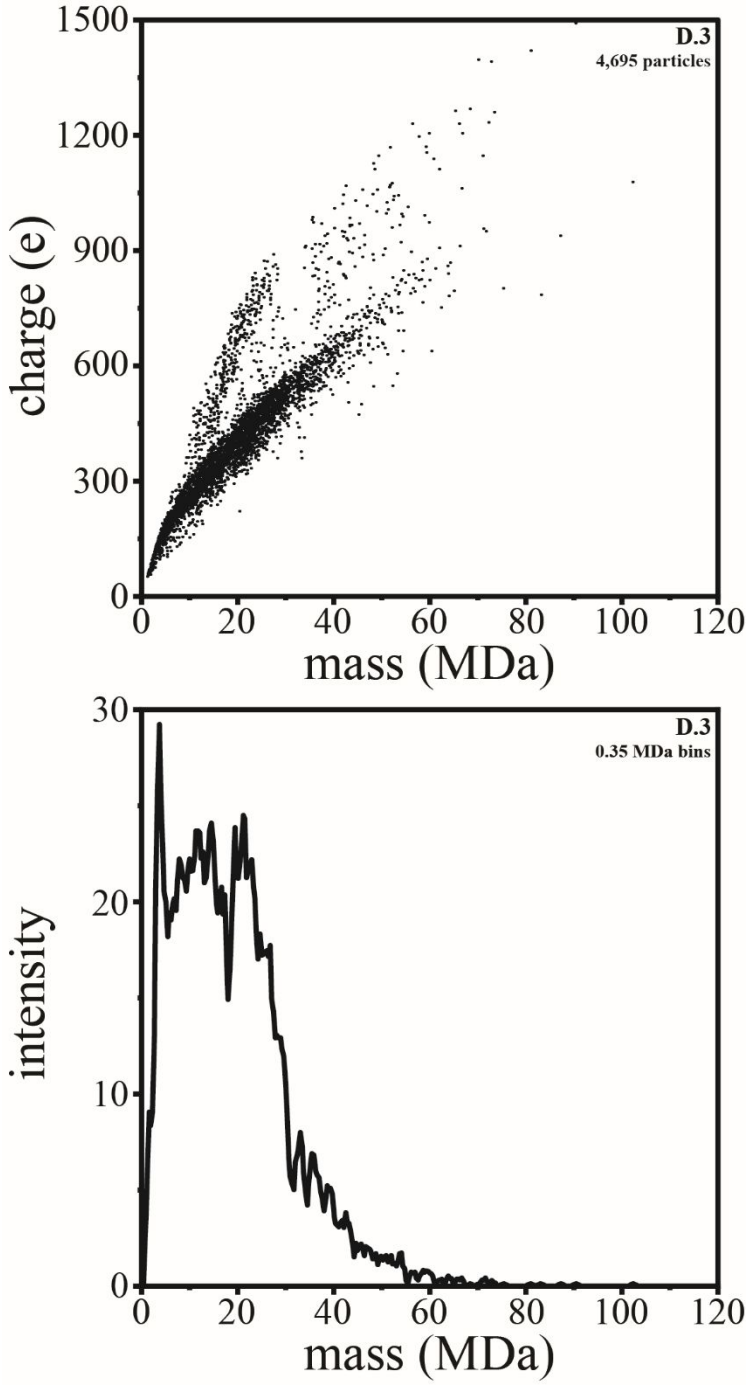

Figure S10. (Top) Mass versus charge CDMS measurement for diabetic (D.3) exosome sample. (Bottom) Mass spectrum generated upon integrating the ion signal across the charge dimension using 0.35 MDa bins.

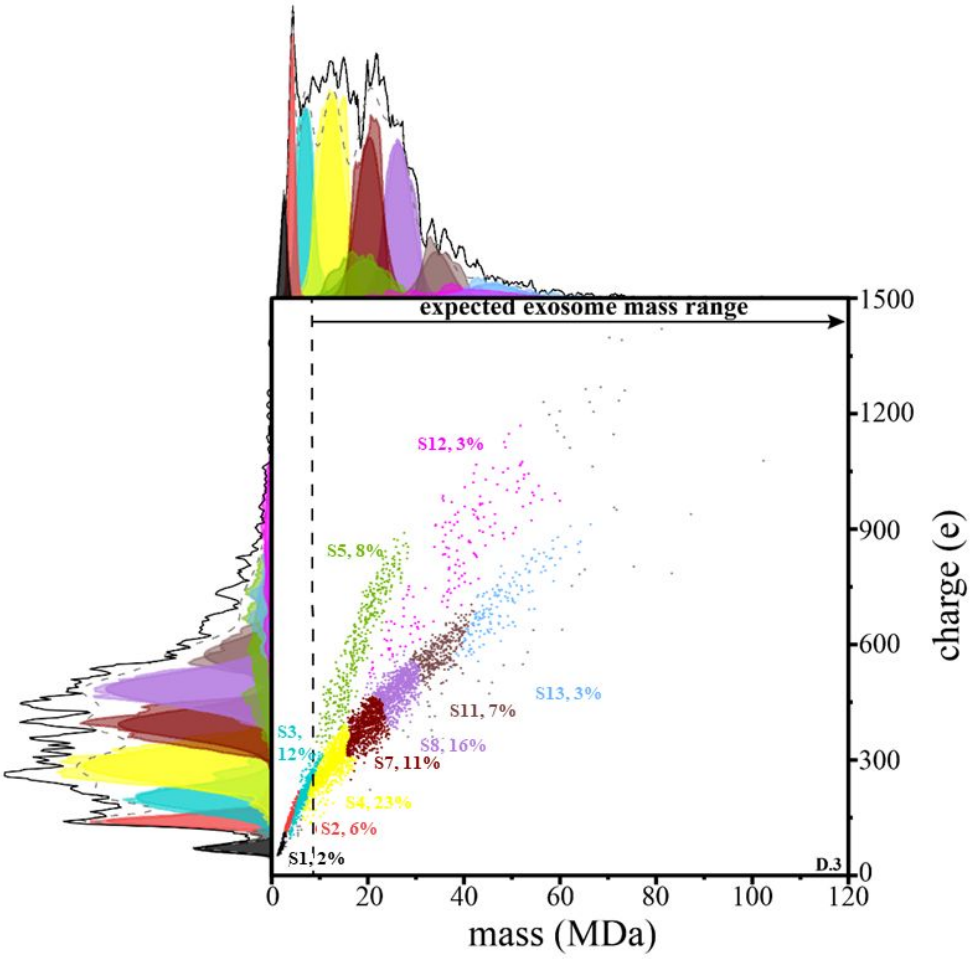

Figure S11. Two-dimensional mass versus charge plot showing subpopulations obtained from Gaussian fits to the experimental data for the third CDMS (D.3) measurement of diabetic murine **Exo$_\kappa$** samples. See main text for details. This model finds evidence for ten subpopulations with abundance greater than 1%. Each point shows the mass and charge measured for a single particle and is assigned to a subpopulation (indicated by color). Subfamily assignment is based on the highest probability of each particle belonging to a specific subfamily. Visually, this leads to boundaries that are artificially strict as in reality the subpopulations overlap. The top and left side traces show the integrated raw data for the mass and charge dimensions, respectively and the corresponding sums of the Gaussian curves as black lines for these dimensions. The determined fits for each subpopulation are also delineated using the same color scheme. The percentage of each subpopulation is also indicated. The dashed vertical line provides an estimate of the delineation between those particles having masses in the range that is expected for exosomes, and those particles that are too small to be exosomes.

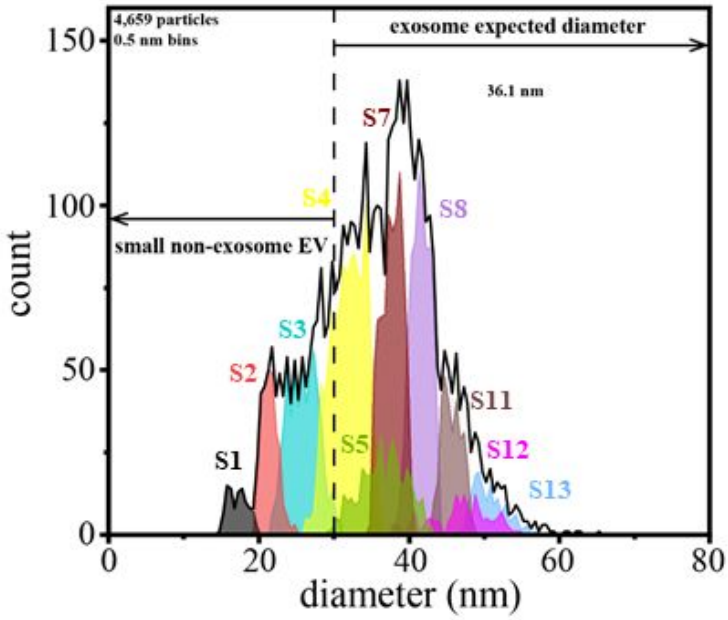

Figure S12. Plot of CDMS-derived diameters for each diabetic sample (D.3) subpopulation (shown in figure S11) using a bin size of 0.5 nm. Particle diameters from CDMS were determined by assuming a spherical geometry and a density of 1.17 g/mL.

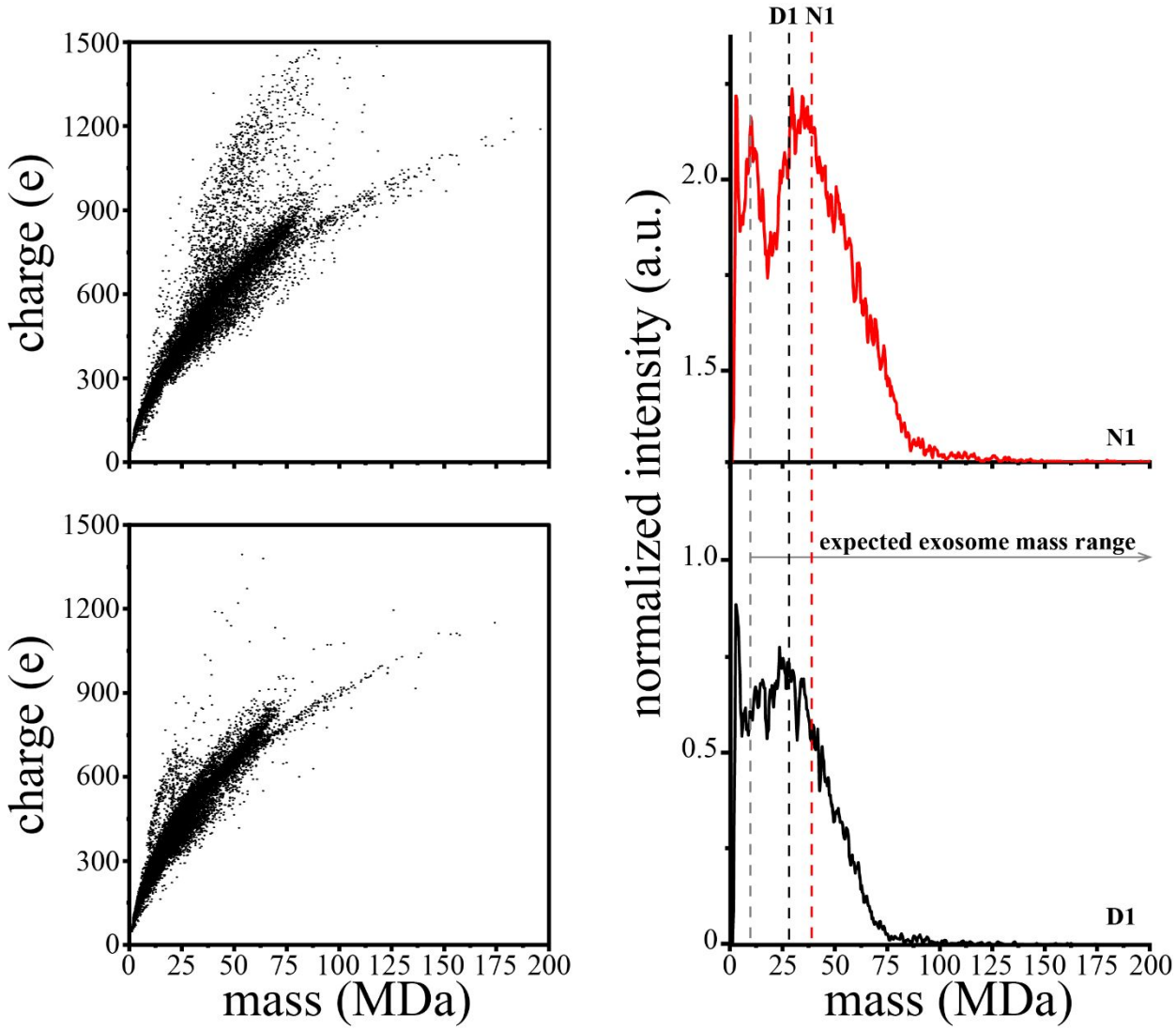

Figure S13. (a) and (b) Mass versus charge CDMS measurements for non-diabetic (N1) and diabetic (D1) wound-edge keratinocyte-derived exosome samples. (c) N1 (red trace) and D1 (black trace) mass spectra generated upon integrating the ion signal across the charge dimension using 0.35 MDa bins. Red (N1) and black (D1) dashed lines mark the average mass. The grey line denotes the expected mass range of exosomes based on assuming a spherical geometry, a 30 nm minimum exosome diameter, and an average density of 1.17 g/mL.

Table SI. Summary of GMM-EM subpopulations upon analysis of the six unprocessed CDMS data leading to the subpopulation resolved data

Subfamily	Sample (Cohort#)	CDMS measurement: ($\overline{m}$, $\overline{z}$)[a], percentage	Average: ($\overline{m}$, $\overline{z}$, percentage)[a]
S1	N,(1)(2)(3)	(2.1 ± 1.9, 79.3 ± 37, 1%), (2.2 ± 1.9, 79.3 ± 33, 1%), (1.4 ± 0.8, 57.1 ± 10, 1%)	(1.83 ± 0.2, 67.5 ± 6.1, 1%)
	D,(1)(2)(3)	(1.7 ± 1.4, 67.0 ± 26, 1%), (1.7 ± 1.4, 79.3 ± 25, 1%), (1.8 ± 1.2, 67.0 ± 23, 2%)	
S2	N,(1)(2)(3)	(3.3 ± 2.8, 132 ± 47, 4%), (3.4 ± 2.8, 136 ± 71, 6%), (3.9 ± 4.0, 142 ± 78, 4%)	(3.4 ± 0.2, 134 ± 4.5, 6%)
	D,(1)(2)(3)	(3.1 ± 1.8, 128 ± 49, 10%), (3.2 ± 2.3, 128 ± 56, 6%), (3.5 ± 1.4, 138 ± 35, 6%)	
S3	N,(1)(2)(3)	(8.7 ± 6.1, 224 ± 98, 10%), (8.5 ± 5.3, 222 ± 94, 6%), (9.3 ± 3.7, 241 ± 71, 6%)	(7.5 ± 1.2, 212 ± 8, 9%)
	D,(1)(2)(3)	(6.1 ± 3.1, 193 ± 82, 9%), (6.4 ± 4.1, 194 ± 82, 10%), (6.3 ± 3.7, 198 ± 74, 12%)	
S4	N,(1)(2)(3)	(15.6 ± 7.8, 304 ± 135, 9%), (14.4 ± 6.6, 304 ± 135, 11%), (14.9 ± 6.4, 314 ± 82, 13%)	(13.4 ± 1.6, 292 ± 14, 15%)
	D,(1)(2)(3)	(11.7 ± 6.1, 274 ± 115, 18%), (11.8 ± 5.7, 274 ± 99, 15%), (11.8 ± 5.9, 282 ± 105, 23%)	
S5	N,(1)(2)(3)	(16.0 ± 7.6, 550 ± 123, 0.3%), (16.8 ± 11, 595 ± 353, 2%), (15.5 ± 11, 573 ± 359, 3%)	(17.6 ± 1.3, 558 ± 80, 3%)
	D,(1)(2)(3)	(18.2 ± 10, 514 ± 288, 3%), (19.9 ± 11, 627 ± 271, 3%), (18.9 ± 9.7, 484 ± 381, 8%)	
S6	N,(1)(3)	(17.0 ± 9, 595 ± 353, 2%), (19.6 ± 12, 433 ± 135, 6%)	(18.3 ± 1.3, 514 ± 80, 4%)
S7	D,(1)(2)(3)	(21.5 ± 6.1, 403 ± 129, 13%), (19.6 ± 6.1, 374 ± 78, 10%), (19.8 ± 6.1, 391 ± 88, 17%)	(20.3 ± 0.9, 390 ± 10.5, 13%)
S8	N,(1)(2)(3)	(26.5 ± 9.6, 422 ± 117, 14%), (22.6 ± 6.6, 391 ± 118, 13%), (24.3 ± 9.6, 415 ± 94, 21%)	(25.5 ± 1.4, 456 ± 46, 16%)
	D,(1)(2)(3)	(27.3 ± 6.1, 470 ± 135, 14%), (26.6 ± 8.5, 460 ± 112, 19%), (26.0 ± 6.2, 575 ± 82, 16%)	
S9	N,(1)(2)(3)	(36.2 ± 9.6, 532 ± 117, 17%), (30.5 ± 6.8, 478 ± 135, 11%), (33.6 ± 7.6, 520 ± 124, 12%)	(33.9 ± 1.4, 513 ± 17.8, 13%)
	D,(1)(2)	(35.1 ± 4.3, 532 ± 170, 7%), (34.3 ± 4.3, 504 ± 153, 5%)	
S10	D,(1)(2)	(38.1 ± 8.2, 572 ± 88, 6%), (42.2 ± 10, 608 ± 88, 9%)	(40.1 ± 2.0, 590 ± 18.0, 8%)
S11	N,(1)(2)(3)	(45.8 ± 6.9, 576 ± 129, 5%), (38.2 ± 6.1, 543 ± 171, 7%), (43.5 ± 9.9, 597 ± 139, 11%)	(41.7 ± 1.5, 588 ± 22.0, 7%)
	D,(1)(2)(3)	(47.5 ± 10, 624 ± 144, 5%), (41.2 ± 7.6, 599 ± 147, 5%), (33.9 ± 7.0, 590 ± 306, 7%)	
S12	N,(1)(2)(3)	(44.3 ± 24, 837 ± 335, 6%), (44.1 ± 28, 790 ± 212, 4%), (47.5 ± 19, 876 ± 300, 3%)	(44.4 ± 1.5, 849 ± 28, 4%)
	D,(2)(3)	(45.2 ± 21, 876 ± 265, 2%), (41.1 ± 12, 864 ± 330, 3%)	
S13	D,(3)	(45.6 ± 19, 710 ± 153, 3%)	
S14	N,(1)(2)	(52.3 ± 14, 673 ± 112, 10%), (50.7 ± 11, 683 ± 131, 9%)	(51.4 ± 1.1, 676 ± 8.4, 9%)
	D,(1)(2)	(49.7 ± 9.4, 661 ± 82, 10%), (52.8 ± 7.2, 685 ± 53, 5%)	
S15*	N,(1)(2)(3)	(53.2 ± 6.9, 629 ± 129, 3%), (50.1 ± 11, 602 ± 124, 12%), (58.4 ± 8.4, 690 ± 135, 3%)	(53.9 ± 3, 640 ± 33, 6%)
S16	D,(1)(2)	(59.6 ± 12, 734 ± 147, 6%), (59.6 ± 11, 729 ± 153, 7%)	(59.6 ± 0, 732 ± 2.6, 7%)
S17	N,(1)	(66.1 ± 10, 680 ± 106, 3%)	
S18	N,(1)(2)	(68.2 ± 17, 789 ± 117, 10%), (66.5 ± 12, 799 ± 141, 6%)	(67.3 ± 0.8, 794 ± 4.9, 8%)
S19	N,(1)(2)(3)	(66.3 ± 31, 1216 ± 129, 2%), (70.1 ± 30, 1228 ± 271, 3%), (70.7 ± 25, 1228 ± 98, 4%)	(69.0 ± 2.2, 1224 ± 5.5, 3%)
S20	N,(1)(2)	(95.6 ± 31, 842 ± 129, 2%), (101 ± 131, 894 ± 135, 2%)	(90.3 ± 8.2, 849 ± 22, 2%)
	D,(1)(2)	(82.1 ± 24, 830 ± 141, 2%), (82.1 ± 153, 832 ± 153, 2%)	

[a] $\overline{m}$ is the peak center from extracted mass subpopulations fit with Gaussians given in units of MDa, $\overline{z}$ is the peak center from extracted charge populations fit with Gaussians given in units of e, percent total ions is calculated based on the total number of ions collected per CDMS measurement, the error is reported as the goodness of fit of the individual Gaussians. Reported as the average of each subpopulation across all four density fractions.

[b] percentage is calculated based on normalized average across CDMS measurements observed for each individual subpopulation, the error reported is the standard deviation from the mean.

References for Supplemental Information:

1 Zhou, X. *et al.* Exosome-Mediated Crosstalk between Keratinocytes and Macrophages in Cutaneous Wound Healing. *ACS Nano* **14**, 12732-12748, doi:10.1021/acsnano.0c03064 (2020).

2 Brown, B. A. *et al.* Charge Detection Mass Spectrometry Measurements of Exosomes and other Extracellular Particles Enriched from Bovine Milk. *Anal Chem* **92**, 3285-3292, doi:10.1021/acs.analchem.9b05173 (2020).

3 Contino, N. C., Pierson, E. E., Keifer, D. Z. & Jarrold, M. F. Charge Detection Mass Spectrometry with Resolved Charge States. *Journal of the American Society for Mass Spectrometry* **24**, 101-108, doi:10.1007/s13361-012-0525-5 (2013).

4 Pierson, E. E., Contino, N. C., Keifer, D. Z. & Jarrold, M. F. Charge Detection Mass Spectrometry for Single Ions with an Uncertainty in the Charge Measurement of 0.65 e. *Journal of the American Society for Mass Spectrometry* **26**, 1213-1220, doi:10.1007/s13361-015-1126-x (2015).

5 Pierson, E. E., Keifer, D. Z., Contino, N. C. & Jarrold, M. F. Probing higher order multimers of pyruvate kinase with charge detection mass spectrometry. *International Journal of Mass Spectrometry* **337**, 50-56, doi:https://doi.org/10.1016/j.ijms.2013.01.002 (2013).

6 Keifer, D. Z., Shinholt, D. L. & Jarrold, M. F. Charge Detection Mass Spectrometry with Almost Perfect Charge Accuracy. *Anal Chem* **87**, 10330-10337, doi:10.1021/acs.analchem.5b02324 (2015).

7 Draper, B. E., Anthony, S. N. & Jarrold, M. F. The FUNPET—a New Hybrid Ion Funnel-Ion Carpet Atmospheric Pressure Interface for the Simultaneous Transmission of a Broad Mass Range. *Journal of The American Society for Mass Spectrometry* **29**, 2160-2172, doi:10.1007/s13361-018-2038-3 (2018).

8 Doussineau, T. *et al.* Charging megadalton poly(ethylene oxide)s by electrospray ionization. A charge detection mass spectrometry study. *Rapid Communications in Mass Spectrometry* **25**, 617-623, doi:https://doi.org/10.1002/rcm.4900 (2011).

9 Elliott, A. G., Harper, C. C., Lin, H. W. & Williams, E. R. Mass, mobility and MS(n) measurements of single ions using charge detection mass spectrometry. *Analyst* **142**, 2760-2769, doi:10.1039/c7an00618g (2017).

10 Pierson, E. E. *et al.* Detection of late intermediates in virus capsid assembly by charge detection mass spectrometry. *J Am Chem Soc* **136**, 3536-3541, doi:10.1021/ja411460w (2014).

11 Doussineau, T. *et al.* Charge Detection Mass Spectrometry for the Characterization of Mass and Surface Area of Composite Nanoparticles. *The Journal of Physical Chemistry C* **119**, 10844-10849, doi:10.1021/jp510081v (2015).

12 Contino, N. C. & Jarrold, M. F. Charge detection mass spectrometry for single ions with a limit of detection of 30 charges. *International Journal of Mass Spectrometry* **345-347**, 153-159, doi:https://doi.org/10.1016/j.ijms.2012.07.010 (2013).

13 Benner, W. H. A Gated Electrostatic Ion Trap To Repetitiously Measure the Charge and m/z of Large Electrospray Ions. *Analytical Chemistry* **69**, 4162-4168, doi:10.1021/ac970163e (1997).

14 Doussineau, T. *et al.* Frontispiece: Mass Determination of Entire Amyloid Fibrils by Using Mass Spectrometry. *Angewandte Chemie International Edition* **55**, doi:https://doi.org/10.1002/anie.201680761 (2016).

15 Fuerstenau, S. D. & Benner, W. H. Molecular weight determination of megadalton DNA electrospray ions using charge detection time-of-flight mass spectrometry. *Rapid Commun Mass Spectrom* **9**, 1528-1538, doi:10.1002/rcm.1290091513 (1995).
16 Hogan, J. A. & Jarrold, M. F. Optimized Electrostatic Linear Ion Trap for Charge Detection Mass Spectrometry. *Journal of The American Society for Mass Spectrometry* **29**, 2086-2095, doi:10.1007/s13361-018-2007-x (2018).
17 Keifer, D. Z., Motwani, T., Teschke, C. M. & Jarrold, M. F. Measurement of the accurate mass of a 50 MDa infectious virus. *Rapid Commun Mass Spectrom* **30**, 1957-1962, doi:10.1002/rcm.7673 (2016).
18 Keifer, D. Z., Pierson, E. E. & Jarrold, M. F. Charge detection mass spectrometry: weighing heavier things. *Analyst* **142**, 1654-1671, doi:10.1039/C7AN00277G (2017).
19 Lutomski, C. A. *et al.* Hepatitis B Virus Capsid Completion Occurs through Error Correction. *J Am Chem Soc* **139**, 16932-16938, doi:10.1021/jacs.7b09932 (2017).
20 Motwani, T. *et al.* A viral scaffolding protein triggers portal ring oligomerization and incorporation during procapsid assembly. *Sci Adv* **3**, e1700423, doi:10.1126/sciadv.1700423 (2017).
21 Shelton, H., Jr., C. D. H. & Wuerker, R. F. Electrostatic Acceleration of Microparticles to Hypervelocities. *Journal of Applied Physics* **31**, 1243-1246, doi:10.1063/1.1735813 (1960).
22 Gallego-Perez, D. *et al.* Topical tissue nano-transfection mediates non-viral stroma reprogramming and rescue. *Nat Nanotechnol* **12**, 974-979, doi:10.1038/nnano.2017.134 (2017).
23 Roy, S. *et al.* Neurogenic tissue nanotransfection in the management of cutaneous diabetic polyneuropathy. *Nanomedicine* **28**, 102220, doi:10.1016/j.nano.2020.102220 (2020).
24 Ghatak, S. *et al.* AntihypoxamiR functionalized gramicidin lipid nanoparticles rescue against ischemic memory improving cutaneous wound healing. *Nanomedicine : nanotechnology, biology, and medicine* **12**, 1827-1831, doi:10.1016/j.nano.2016.03.004 (2016).
25 Ahmed, N. S. *et al.* Epidermal E-Cadherin Dependent beta-Catenin Pathway Is Phytochemical Inducible and Accelerates Anagen Hair Cycling. *Mol. Ther.* **25**, 2502-2512, doi:10.1016/j.ymthe.2017.07.010 (2017).
26 Chopra, N. et al. Biophysical Characterization and Drug Delivery Potential of Exosomes from Human Wharton's Jelly-Derived Mesenchymal Stem Cells. ACS Omega 4, 13143-13152, doi:10.1021/acsomega.9b01180 (2019).